JOURNAL OF GEOPHYSICAL RESEARCH: ATMOSPHERES, VOL. 118, 9673–9689, doi:10.1002/jgrd.50776, 2013

# Rain characteristics and large-scale environments of precipitation objects with extreme rain volumes from TRMM observations

Yaping Zhou,[1] William K. M. Lau,[2] and Chuntao Liu[3]

Received 3 May 2013; revised 21 August 2013; accepted 22 August 2013; published 10 September 2013.

[1] This study adopts a "precipitation object" approach by using 14 years of Tropical Rainfall Measuring Mission (TRMM) Precipitation Feature (PF) and National Centers for Environmental Prediction (NCEP) reanalysis data to study rainfall structure and environmental factors associated with extreme heavy rain events. Characteristics of instantaneous extreme volumetric PFs are examined and compared to those of intermediate and small systems. It is found that instantaneous PFs exhibit a much wider scale range compared to the daily gridded precipitation accumulation range. The top 1% of the rainiest PFs contribute over 55% of total rainfall and have 2 orders of rain volume magnitude greater than those of the median PFs. We find a threshold near the top 10% beyond which the PFs grow exponentially into larger, deeper, and colder rain systems. NCEP reanalyses show that midlevel relative humidity and total precipitable water increase steadily with increasingly larger PFs, along with a rapid increase of 500 hPa upward vertical velocity beyond the top 10%. This provides the necessary moisture convergence to amplify and sustain the extreme events. The rapid increase in vertical motion is associated with the release of convective available potential energy (CAPE) in mature systems, as is evident in the increase in CAPE of PFs up to 10% and the subsequent dropoff. The study illustrates distinct stages in the development of an extreme rainfall event including (1) a systematic buildup in large-scale temperature and moisture, (2) a rapid change in rain structure, (3) explosive growth of the PF size, and (4) a release of CAPE before the demise of the event.

**Citation:** Zhou, Y., W. K. M. Lau, and C. Liu (2013), Rain characteristics and large-scale environments of precipitation objects with extreme rain volumes from TRMM observations, *J. Geophys. Res. Atmos.*, *118*, 9673–9689, doi:10.1002/jgrd.50776.

## 1. Introduction

[2] One of the most likely consequences of global warming is an increase in extreme weather events, such as droughts, floods, and heat waves [*IPCC*, 2012]. A number of recent studies have shown increased frequency and intensity of extreme precipitation events in recent decades [*Easterling et al*., 2000; *Trenberth et al*., 2003; *Groisman et al*., 2005; *Lau and Wu*, 2007; *Allan and Soden*, 2008; *Min et al*., 2011]. Unlike the global mean precipitation, which is constrained by the global radiative convective balance and increases at a rate (~3% $°C^{-1}$) much slower than the atmospheric water vapor (~7% $°C^{-1}$) [*Allen and Ingram*, 2002; *Held and Soden*, 2006], extreme precipitation is more closely related to moisture convergence in the atmosphere and increases at a much faster rate than the mean precipitation [*Kharin et al*., 2007; *O'Gorman and Schneider*, 2009; *Lau and Wu*, 2011; *Lau et al*., 2013].

[3] However, it is a challenge to pin down the direct connection of an individual extreme precipitation event to global warming. Extreme precipitation occurs under a variety of mesoscale and synoptic meteorological conditions. Many extreme precipitation events can be identified with mesoscale convective systems (MCSs), such as tropical storms and hurricanes [*Shepherd et al*., 2007; *Lau et al*., 2008], squall lines, the organization of mesoscale convective complex (MCC), and heavy-precipitation supercells that often produce flash floods [*Moore et al*., 2003; *Smith et al*., 2001]. Extreme precipitation can also result from terrain-forced convection [*Petersen et al*., 1999; *Pontrelli et al*., 1999] and from both strongly and weakly forced synoptic systems [*Maddox et al*., 1979; *Heideman and Fritsch*, 1988; *Bradley and Smith*, 1994]. Despite this, extreme precipitation is usually a result of many coincident meteorological conditions, such as a buildup of large local atmospheric instability or persistent large-scale moisture transport and convergence [*Reale et al*., 2012]. Orographic forcing plays a significant role in many cases, such as the disastrous flooding caused by Typhoon Morakot in 2009 in Taiwan [*Ge et al*., 2010; *Lee et al*., 2011] and rainstorms in 2010 in Pakistan [*Houze*

[1]GESTAR, Morgan State University, Greenbelt, Maryland, USA.
[2]Laboratory for Atmospheres, NASA Goddard Space Flight Center, Greenbelt, Maryland, USA.
[3]Department of Physical and Environmental Sciences, Texas A & M University at Corpus Christi.

Corresponding author: Y. Zhou, GESTAR, Morgan State University, Greenbelt, MD 20771, USA. (yaping.zhou-1@nasa.gov)


2169-897X/13/10.1002/jgrd.50776

*et al*., 2011]. The interaction of the storm's large-scale environment and life cycle is very important and unique to each extreme event and deserves careful study. However, detailed study is impossible for every extreme event because of the lack of thermodynamic observations of the entire storm life cycle and the large number of such events. Moreover, even a detailed case study may not be able to illuminate the connection of individual events to changes in large-scale environments that are attributable to global warming, as in the case of the Pakistan flood in 2010 [*Wang et al*., 2011; *Lau and Kim*, 2012; *Dole et al*., 2011] and Typhoon Morakot [*Lee et al*., 2011].

[4] Therefore, regardless of whether or not the cause is global warming, extreme events are always related to changes in the large-scale environment and local feedback processes that amplify their development. In this study, we use a composite technique to examine the basic characteristics of extreme precipitation and the associated mean large-scale environment in order to gain insight on the changing rain structure and the environmental conditions that are more likely to produce extreme events. Section 2 describes the data set and methodology. Section 3 shows rain characteristics for different sizes of precipitation objects. Section 4 examines mean large-scale environments associated with extreme precipitation events. A summary and discussion is provided in section 5.

## 2. Data and Methodology

[5] The Tropical Rainfall Measuring Mission (TRMM) has accumulated more than 14 years of state-of-the-art tropical rainfall products including rain rates, types, structures, latent heating profiles, and related water vapor and cloud properties. These data products offer a unique opportunity for research on extreme precipitation characteristics and their modulation by climate processes. Here we use the University of Utah Precipitation Feature (PF) database [*Liu et al*., 2008], which provides rainfall characteristics for individual precipitation objects defined by grouping contiguous satellite rainy pixels with related cloud and precipitation observations. This database was developed within the framework of PFs earlier defined by *Nesbitt et al*. [2000] and was updated with version 7 of TRMM products. The characteristics of each PF event, which include the raining area, total rain volume, cloud top temperature inferred from infrared brightness temperature, precipitation radar echo top height, lightning flash rates, etc., are derived from collocated measurements and retrievals from the Precipitation Radar (PR), TRMM Microwave Imager (TMI), Visible and Infrared Sensor, and Lightning Imaging System. This database covers the entire TRMM period (1998 to present) from 36°S to 36°N, enabling quick identification of specific cloud and precipitation systems and characterization of these systems from multiple TRMM instruments. The surface meteorology and vertical profiles of temperature, geopotential height, wind, and humidity associated with each PF were extracted from associated six hourly 2.5° × 2.5° National Centers for Environmental Prediction (NCEP) reanalysis [*Liu et al*., 2008; *Kalnay et al*., 1996; *Kistler et al*., 2001]. The NCEP data were first temporally interpolated to the PF time, and the nearest grid point to the center of the PF was selected for each PF. In this study we use a level-2 radar-based PF data set that was defined by grouping contiguous raining pixels indicated by PR retrievals [*Iguchi et al*., 2000, 2009]. Each PF in the data set has at least four continuous PR pixels with nonzero surface rainfall to remove detection noise. We focus on the PFs with extreme values of volumetric rainfall from PR retrievals and associate them with the large-scale environments from collocated NCEP reanalysis data.

[6] The precipitation feature database is similar to the cloud object approach developed at NASA Langley Research Center to study the cloud and radiation characteristics of various cloud objects, i.e., deep convective clouds or shallow clouds [*Xu et al*., 2005, 2007; *Eitzen and Xu*, 2005]. Composite and clustering techniques were used in the cloud object studies to categorize cloud properties in different types of clouds. *Lin et al*. [2006, 2007] have studied the effect of environmental conditions on tropical deep convective systems observed from the TRMM satellite and have found that not only rainfall rate but also rainfall efficiency increases with sea surface temperature. Although different names are used, both groups use an object-oriented approach that treats continuous satellite footprints of cloud or precipitation areas as a single object with physical and statistical properties. Our study based on PF data could also be viewed as a study of precipitation objects.

[7] In addition to the PF data, we use the TRMM 3B42 [*Huffman et al*., 2007] daily rainfall product to provide additional information for the time-accumulated rainfall information for the grid box where PF locates. The 3B42 algorithm merges precipitation estimates from passive microwave (PMW) products from TRMM TMI and Special Sensor Microwave Imager (SSM/I) and rain estimates from geostationary infrared (IR) products. The SSM/I data are calibrated to the TMI measurements, while the IR estimates are calibrated with PMW estimates. The daily 3B42 data are aggregated from the original three-hourly temporal resolution with 0.25° × 0.25° spatial resolution covering a latitudinal domain from 50°S to 50°N.

[8] The definition of extreme precipitation is highly dependent on the application and data set available. Depending on applications, various indices have been used, e.g., maximum 1 or 5 day precipitation, daily intensity index, or the number of heavy and consecutive precipitation days [*Zhang et al*., 2011]. Different authors define extreme thresholds based on different percentiles of the precipitation distributions, with the farther tail indicating more extreme events. In this study, we define extreme events using the volumetric rain rate (VRR: a product of instantaneous rain intensity and the size of the rain system) from PR near-surface rain [*Iguchi et al*., 2000, 2009] of PFs to focus on the total rain amount the system produces at the TRMM overpass time. VRR pertains to an instantaneous and intrinsic measure of the rainfall intensity that approximates total latent heat release of the system at any instant. Using VRR as a measure of rain intensity, we gain an in-depth perspective of the fundamental physical processes governing the occurrence of extreme precipitation events. The correlation of extreme PF with daily extreme rainfall from TRMM 3B42 data will be discussed in section 3.2.

[9] We also point out that extreme PFs defined based on VRR are focused on storm extent in size and rain amount rather than storm convective intensity, which is characterized by strong updrafts, high lightning rates, and elevated radar reflectivity [*Zipser et al*., 2006].

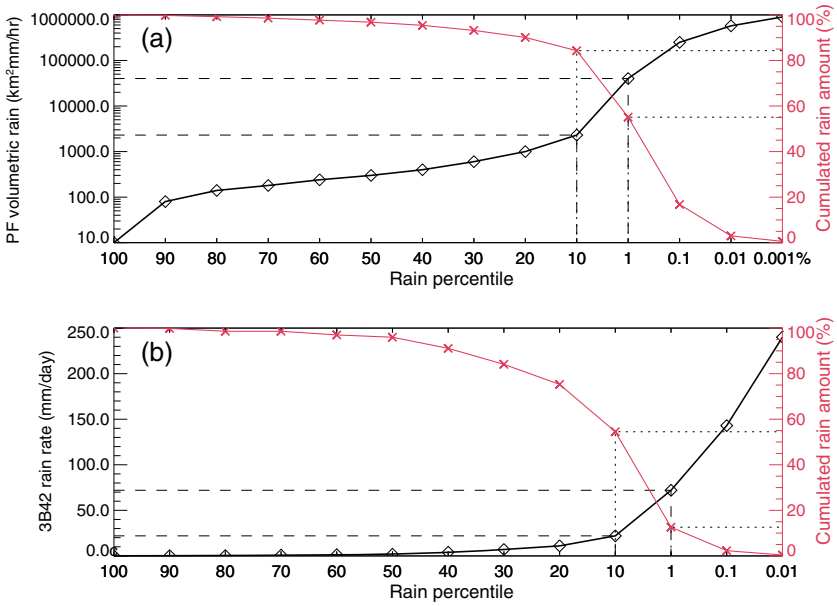


**Figure 1.** (a) Volumetric rain thresholds (left *y* axis, line with diamond) and percentage of cumulative rain amount (right *y* axis, line with cross) with percentiles in rain volume. The percentile represents the percentage of PFs above the threshold over all PFs in 36°S–36°N during 1998–2011. (b) Similar plot as Figure 1a but using nonzero 0.25° × 0.25° grid 3B42 data in 36°S–36°N during 1998–2011.

## 3. Results

### 3.1. Probability Distributions of PF Rainfalls

[10] One advantage of using PF VRR as a reference for extreme rain events is the large data sample based on satellite pixels. There are more than 28 million PFs in the database from January 1998 to December 2011 with a minimum of 4 PR pixels or 75 $km^2$ in size. The smaller systems (less than 4 PR pixels) excluded from the PF database are not expected to contribute to a significant portion of the total rainfall, much less the top 1% of the extreme events [*Liu*, 2011]. To begin, we computed the probability distribution function (PDF) of all PFs according to their VRR and determined the thresholds for every 10% in frequency, as well as the top 1%, 0.1%, 0.01%, and 0.001% for extreme events (Figure 1a). The thresholds increase nonlinearly as the percentile tends toward extreme categories, with an abrupt jump near the top 10th percentile. For example, VRR is less than 2300 mm/h $km^2$ below the top 10th percentile but reaches above 40,000 and 575,000 mm/h $km^2$ in the top 1% and 0.01%, respectively, which is more than 2–3 orders greater than that of median PFs. On the other hand, Figure 1a shows that PFs from the top 1% contribute to over 55% of the total instantaneous rainfall, while those below the 10th percentile (or the lower 90%) contribute less than 20% of the total rainfall. It should be noted that even though the majority (70 ~ 80%) of PFs in Figure 1a are from oceans, the PDFs and the corresponding thresholds from land and oceans separately are extremely close (figure not shown), so only one set of thresholds is used in this study.

[11] Since both rain rate and volumetric rain rate of PF are snapshot measurements, it is interesting to know how those snapshots translate into the time-integrated rain rate. The daily 3B42 data from TRMM [*Huffman et al.*, 2007] contain enough samples (some microwave overpasses and continuous IR) to represent daily rain accumulation fairly well. Physically speaking, a large rainy system usually lives for a long time and brings a heavy rainfall accumulation locally. Therefore, a snapshot of large rainy systems from TRMM would be very likely to lead to a heavy accumulation event in daily precipitation. However, a small system with an intense rain rate locally does not necessarily lead to a heavy rainfall accumulation due to a potentially short lifetime. On the other hand, a heavy daily accumulation event can be from a relatively small system lasting a long time period due to continuous moisture supply, e.g., orographic lifting of monsoonal flow. In order to provide context and contrast PF VRR data with time-integrated precipitation data, we show similar statistical and spatial distribution plots for the daily 3B42 data.

[12] Figure 1b shows a more linear curve of the PDF for the daily 3B42 data than the PF data. The top 1% of the daily gridded precipitation contributes only 13% of the total rainfall versus 55% in the case of the instantaneous PF. Compared to the 3B42 time-averaged gridded data, the PF-based PDF shows that instantaneous rainfall has a larger scale range, with a much longer tail at the extreme end of the distribution. Despite the low frequencies for those above the top 1%, the absolute number of extreme PFs is still quite large due to the enormous total PFs globally (Figure 2), providing a sound basis for our statistical analysis.

### 3.2. Geographical Distributions of Extreme PFs

[13] The geographical distributions of the most extreme rainy PFs in VRR (Figure 2, top) differ significantly from those of the most intense storms [*Zipser et al.*, 2006, Figure 3] and most intense daily rainfall (Figure 2, bottom). The most intense storm was defined by the strength of convection; therefore, elevated high reflectivity, high lightning rate, and strong ice signature at microwave channels (i.e., minimum 85PCT) were used as the main criteria to identify

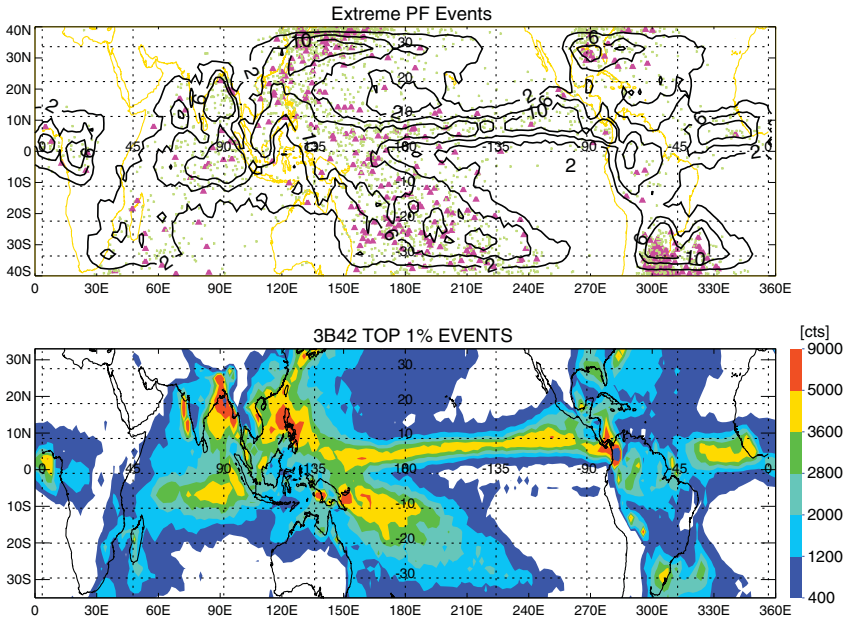


**Figure 2.** (top) Geographical distribution of PFs with extreme volumetric rain. Contours are for population of top 1% of extreme PFs in 2° × 2° grid boxes. TRMM sampling bias has been removed in the population contours by dividing the ratio of actual and mean sample numbers in the grid box. Green, purple, and black triangles are the locations of the top 0.1%, 0.01%, and 0.001% extreme PFs. Note that there are more triangles at subtropics partially due to the sample biases near 30° latitudes. (bottom) Number of top 1% events in 2° × 2° grid boxes (> 72 mm/d) from daily 3B42 data during 1998–2011.

the most intense storms. Figure 2 (top) shows that most of the extreme rainy PFs in VRR occur over the oceans as opposed to over the land regions in the case of severe storms. High concentrations of systems with extreme volumetric rain can be seen over the Northwest Pacific, South Pacific Convergence Zone (SPCZ), Northwest Atlantic, and the Bay of Bengal, accompanied by moderate concentrations along the tropical Intertropical Convergence Zone (ITCZ). Over land, large volumetric PFs are found along the coastal South China Sea and the southeast U.S. as a result of tropical storms moving in from the oceans and large moisture transport from the sea. High concentrations of extreme PFs are also found over South America south of the Tropic of Capricorn—the same region frequented by intense storms [*Zipser et al*., 2006].

[14] It is important to understand the relationship between extreme PFs in VRR and extreme precipitation accumulation events at the surface, since the former only captures an instantaneous snapshot while the latter requires rainfall over a certain duration. Figure 2 (bottom) shows the geographical distribution of the top 1% of extreme daily events (daily precipitation greater than 72 mm/d) based on the 3B42 data. The most frequent occurrences of daily extreme rainfall are found over the northwest Pacific and South China Sea along the tropical typhoon route, SPCZ, the Pacific and eastern Atlantic ITCZ, the Bay of Bengal, Gulf of Mexico, Southwest U.S., Central Amazon, northeast Argentina, and the Gulf of Guinea. It is obvious that regions with high concentrations of extreme PFs also have a high frequency of daily extreme events. However, Figure 2 (top) shows extreme PF events quite evenly spread out in the equatorial Indian Ocean, west Pacific, and SPCZ region (even for the very extreme ones), while the 3B42 map (Figure 2, bottom) shows regions of high concentration of extreme events at the center of SPCZ and equatorial ITCZ. Also from Table 1, many extreme PFs do not produce extreme daily rainfall. This evidence shows that many extreme PFs do not last long enough to produce large rain accumulation. The meteorological conditions used to produce extreme PF quickly dissolve. This indicates that an extreme daily precipitation accumulation event might require a more rigorous environment and higher level of organization of the precipitation system. Particularly worth noticing is the high frequency of daily extreme rainfall off the west coast of India and the southeast coast of Asia as a result of the orographic effect.

[15] To obtain a more quantitative measure, we collocated top PFs and their corresponding daily mean precipitations from 3B42 and calculated the percentage of top PFs that produced daily extreme rainfall (Table 1). It was found that only about 17% of PFs in the top 1% were associated with heavy daily events (greater than 50 mm/d). This rises to 36.4% and 54.9% for the top 0.1% and 0.01% of PFs, respectively. Since many of the large rain systems span over night, we also computed 3 day rain accumulation centered with the PFs. The percentage of cases with 3 day rain accumulation greater than 50 mm rises to 40.3%, 61.5%, and 77.2% for PFs in the top 1%, 0.1%, and 0.01%, respectively, which is consistently larger than that of 1 day accumulation. These results indicate that larger PFs usually last longer, as shown in *Liu* [2011], and many of the extreme PFs extend over more than 1 day. The above results show that extreme PFs (especially for those above top 0.1%) are most likely associated with large accumulated rain events, so the results shown in this study will generally apply to extreme events in time-averaged measurements (a day or shorter). Of course, there are instances of

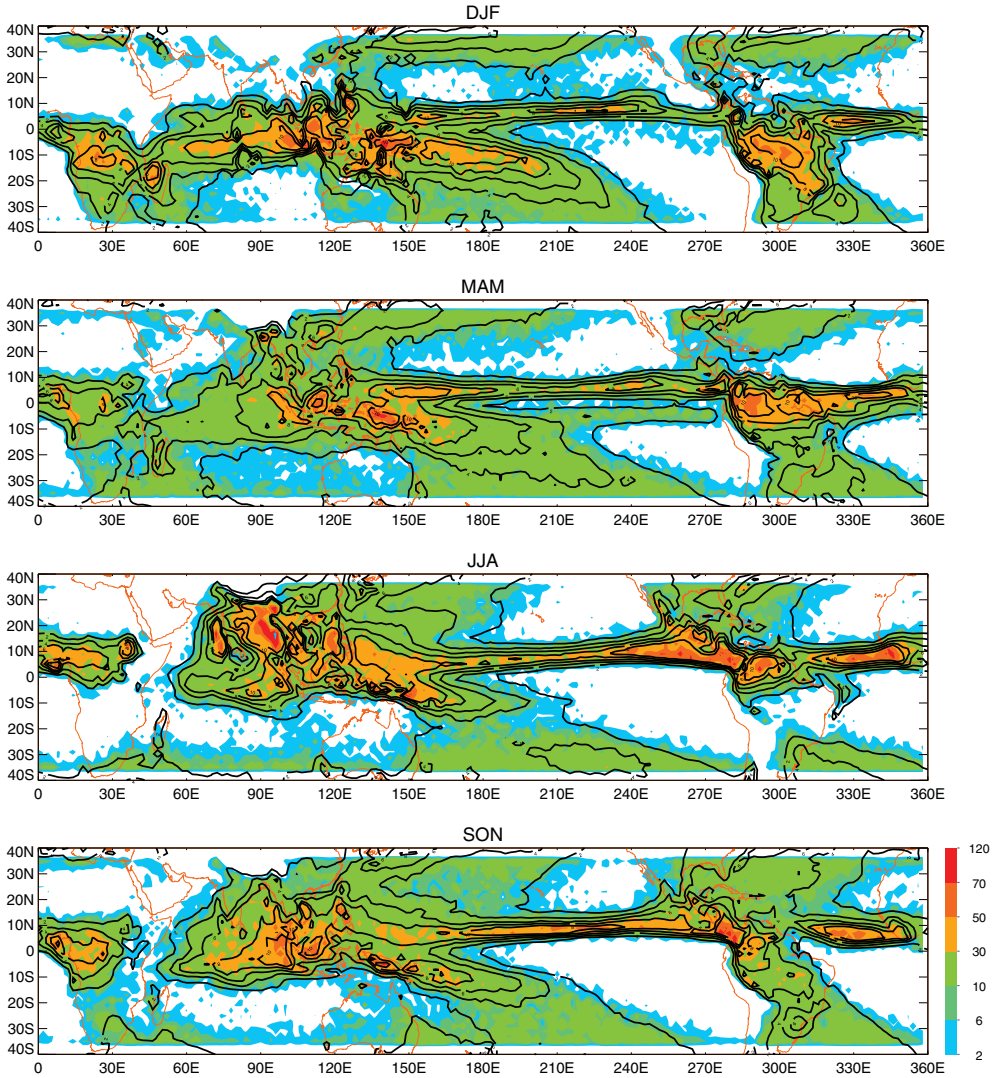


**Figure 3.** Normalized total number of top 1% extreme PFs (shading) in 2° × 2° grid boxes and mean precipitation from 3B42 data (contour) in each season. TRMM sampling bias has been removed by dividing the ratio of actual and mean sample numbers in the grid box.

large instantaneous rain showers from short-lived systems, such as afternoon showers in deep tropical land areas, that are captured by extreme PFs but do not produce heavy daily rainfall [*Takayabu et al*., 2012]. On the other hand, heavy daily rainfalls could be the result of persistent moderate rain throughout the day [*Liu*, 2011].

### 3.3. MCS and Extreme PF

[16] While it is likely that extreme volumetric PFs are also large in size (see Figure 5 for more detailed discussion), here we will examine what kind of rain systems (e.g., MCS, warm rain system, or others) are found in different percentiles of PF. MCS is one of the dominant heavy-precipitation systems in the tropics, with complex organized storms that extend more than 100 km in one direction but are smaller than extratropical cyclones [*Houze and Churchill*, 1987]. Tropical cyclones are one of such systems that contribute more than 60% of the total extreme events in northwest Pacific based on pentad Global Precipitation Climatology Program data [*Lau et al*., 2008]. Other MCSs include MCC, squall lines, lake-effect snow events, and polar lows. Based on 1 year of SSM/I data, *Mohr et al*. [1999] found that MCSs consisted about 10%–20% of the sampled systems by number but contributed 70%–80% of the rainfall throughout the Tropics. Using a similar MCS definition (PF size > 2000 km$^2$) as *Mohr et al*. [1999], we find that very few PFs below the top 10th percentile are contributed by MCS simply due to the size requirement by the definition (Table 2). About 79.6% and 67.8% of the PFs in the top 1% have one or several MCSs imbedded in the system over the land and the oceans, respectively. For those at the top 0.1%, a larger percentage (90%)

**Table 1.** Percentage of Top PFs With 1 and 3 Day Precipitation Accumulation Centered at PF Locations and Times From TRMM 3B42 Greater Than 50 mm/d

| | 1 Day Accumulation >50 mm | 3 Day Accumulation >50 mm |
|---|---|---|
| Top 1% | 17.0% | 40.3% |
| Top 0.1% | 36.4% | 61.5% |
| Top 0.01% | 54.9% | 77.2% |

**Table 2.** Fraction of PFs Categorized by Volumetric Rainfall That Are Identified as MCSs[a]

| | <10% | 10% | 1% | 0.1% | 0.01% | 0.001% |
|---|---|---|---|---|---|---|
| Land | 0.0 | 5.2 | 82.7 | 93.9 | 98.4 | 100.0 |
| Ocean | 0.0 | 2.7 | 72.0 | 91.1 | 96.7 | 99.6 |
| Global | 0.0 | 3.5 | 74.8 | 91.7 | 97.0 | 99.7 |

[a]With size > 2000 $km^2$.

could be characterized with MCS globally, with an even higher percentage over some land regions; i.e., 99% of the PFs in the top 0.1% are identified as MCSs in the Bay of Bengal and in equatorial West Africa. These results indicate a much lower percentage (about 3 ~ 4%) of MCS in all PFs compared with the results of *Mohr et al*. [1999]. There are a few explanations for this discrepancy. The SSM/I single pixel size is $13 \times 15\ km^2$, larger than the smallest PF ($75\ km^2$) in this study, which could lead to some small systems missing from *Mohr et al*. [1999] that are detectable by PR. More importantly, however, studies using SSM/I rely on the ice scattering signal, which detects the deep convection with ice but totally misses warm rain systems as a result. Therefore, the total population of systems in *Mohr et al*. [1999] would be smaller due to missing warm rain systems, especially over the oceans.

[17] Even though it has been shown that most warm rain systems are small in size [*Liu and Zipser*, 2009], it is not clear what percentage of the PFs in each volumetric rain category belongs to warm rain systems or whether warm rain can also produce extreme rainfall. Defining warm rain events as those that have a minimum IR temperature greater than 273 K, a minimum 85 GHz PCT (polarization-corrected brightness temperature) greater than 250 K, and a maximum storm height less than 4.5 km, we find that warm rain events contribute only 1.4% and 0.2% to the top 10th percentile over the oceans and the land, respectively, which means that warm rain events rarely contribute to extreme PFs by rain volume (Table 3). Interestingly, only about one third of the PFs in the 90th–30th percentiles belong to warm rain systems, and an even smaller percentage of PFs in the bottom 10% meet the warm rain definition. Therefore, it is likely that a large number of small size and low volumetric PFs are either isolated small convective cells or patches of PF separated from a large system. On the other hand, a considerable number of PFs (~20% in the top 1% and 10% in the top 0.1%) are of neither MCS nor pure warm rain systems but most likely have mixed features of warm or mixed-phase rain attached to a colder system [*Liu and Zipser*, 2009]. We want to point out that the minimum size of 4 PR pixels ($75\ km^2$) for this study excludes a large number of small warm rain systems, because most of the warm rain systems are less than $30\ km^2$ in size [*Liu and Zipser*, 2009]. Nevertheless, it does not change the conclusion that warm rain contributes very little to extreme volumetric rain events.

### 3.4. Seasonal and Diurnal Distributions of Extreme PF

[18] Seasonal variations of extreme precipitation are similar to seasonal variations of mean precipitation (Figure 3). For example, high concentrations of extreme events are found in the maritime continent and Southeast Asia in June-July-August (JJA) and are associated with the monsoon system. Extreme precipitation associated with the tropical ITCZ and SPCZ is also in proximity to the intensity and spread of the monsoon system. There is a much broader region of heavy mean precipitation and frequent occurrences of extreme PF events in the SPCZ in December-January-February (DJF) and March-April-May than JJA and September-October-November. On the other hand, both the East Pacific and Atlantic ITCZ regions show more extreme PFs in JJA than in DJF. Over land, more extreme events are found over tropical and subtropical South Africa and the Amazon in DJF than in JJA. The seasonal variations of extreme events poleward of 30° in both hemispheres are likely associated with seasonal migration of midlatitude storm tracks. For example, more extreme PFs are found north of 30°N in the Pacific Ocean in the winter than in the summer due to an equatorward migration of the jet stream. These storms are distinct from the tropical systems in the maritime continent and Southeast China Sea, where an elevated number of extreme PFs appear in JJA due to monsoon and tropical cyclones.

[19] To illustrate the diurnal distributions of PFs according to their volumetric rainfall, we computed normalized frequencies for each hour for PFs within 10%, between 10% and 0.1%, and larger than 0.1% in four subregions: tropical land and oceans (20°S–20°N) and subtropical land and oceans (20°N–36°N and 20°S–36°S) as shown in Figure 4. A relatively weak diurnal cycle is found over the oceans compared to over land, as shown by many previous studies [*Nesbitt and Zipser*, 2003; *Bowman et al*., 2005; *Liu and Zipser*, 2008; *Liu*, 2011]. Because land has low heat capacity compared to the ocean, it has a much larger diurnal cycle of surface temperature than the ocean. The diurnal cycle of PFs over land is mostly driven by convective overturning caused by afternoon heating of the surface and the lower boundary layer. However, the oceanic diurnal cycle is considered to be related to the much weaker daytime stabilization of solar heating and night destabilization of radiative cooling at the cloud top [*Kraus*, 1963]. For tropical oceans, smaller systems (<10% and 10%–0.1% categories) show weaker diurnal variations than the larger systems (> 0.1%). They also reach peak frequency earlier in the morning (3 A.M.) than the larger systems (6–9 A.M.). This is consistent with *Nesbitt and Zipser* [2003], who showed that small systems peak at 3 A.M. but the number of MCSs peaks at 7 A.M. over the oceans. The largest diurnal variation occurs for the top 0.1% of PFs; this is probably due to continuous expanding of smaller MCS during the early morning before dying down in the afternoon [*Nesbitt and Zipser*, 2003]. Over the tropical land, the largest diurnal variation occurs in the top 10%–1%, in which surface heating favors medium size afternoon convection. The afternoon peaks are reversed for the extreme PFs (top 0.1%), in which most MCSs prolong into midnight and keep growing until the early morning. The diurnal cycle in subtropical land and

**Table 3.** Fraction of PFs Categorized by Volumetric Rainfall That Are Identified as Warm Rain Systems[a]

| | <90% | 90–30% | 30% | 20% | 10% | >1% |
|---|---|---|---|---|---|---|
| Land | 9.5 | 34.1 | 16.3 | 7.4 | 0.2 | 0.0 |
| Ocean | 12.3 | 38.6 | 19.5 | 9.3 | 1.5 | 0.0 |
| Global | 2.0 | 9.2 | 3.9 | 1.6 | 1.1 | 0.0 |

[a]Minimum infrared brightness temperature > 273 K.

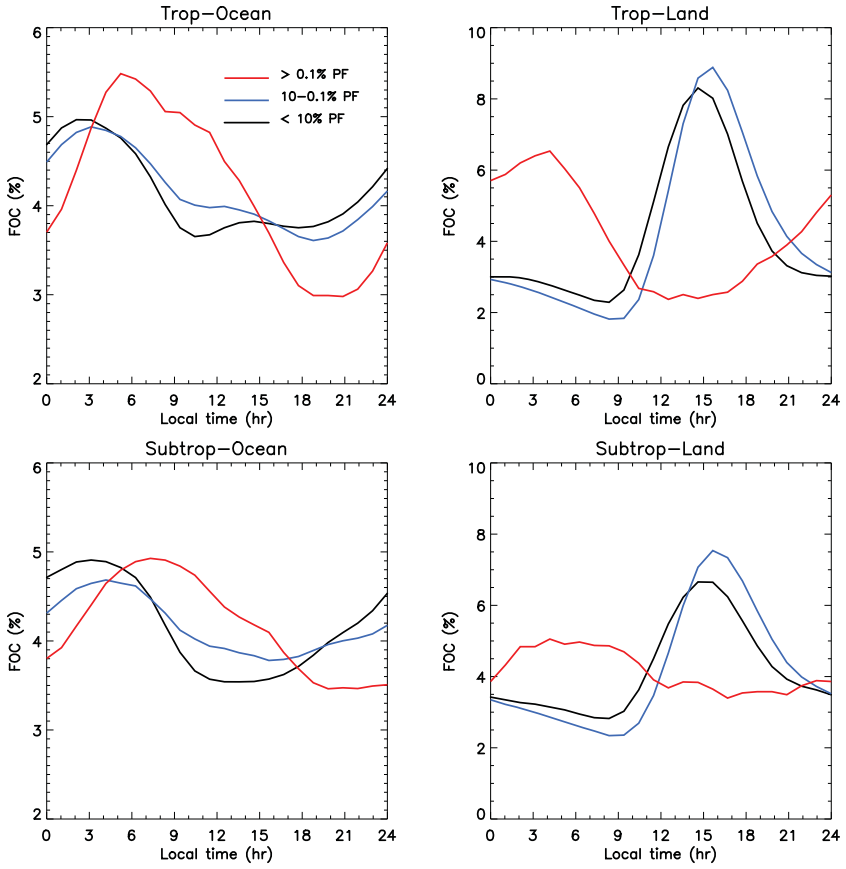


**Figure 4.** Diurnal distributions of the total number of PFs from three PF categories for four subregions: tropical (20°S–20°N) oceans, tropical land, subtropical (20°N–36°N and 20°S–36°S) oceans, and subtropical land.

oceans is similar to the diurnal cycle in the tropics with a relatively smaller magnitude, which means that the difference between the diurnal cycles is mainly due to thermal conditions of the surface between land and ocean. These results are consistent with various previous studies [*Yang and Slingo*, 2001; *Nesbitt and Zipser*, 2003; *Liu and Zipser*, 2008; *Liu*, 2011].

### 3.5. Variations of Rain Size and Rain Rate With VRR

[20] In this subsection, we investigate the relationship between rain size, volume, and mean intensity. In general, total volumetric rain is expected to increase with PF size (Figures 5a and 5b). However, the relationship between VRR and rain size is far from linear, as demonstrated by the broad spread of the PDF (Figures 5a and 5b) and the difference of PDFs in difference subregions (Figures 5c and 5d). For cases below the median VRR, the PF stays predominantly smaller than 150 $km^2$ and is associated with primarily meso-γ or storm-scale systems. Above the median VRR, the size increases rapidly to 1500–5000 $km^2$. Beyond the top 10th percentile, the growth is exponential, with the size increasing 20 times from 5000 to 100,000 mm/h $km^2$ and VRR increasing 2–3 orders (Figure 1). The exponential growth is more due to the rapid increase in size than in the rain rate, as is evident in the near-vertical orientation of the PDF beyond the top 10th percentile.

[21] As seen from Figures 5a and 5b, tropical oceans display a much higher frequency of small PFs (under 150 $km^2$) and moderate VRR (80th–30th percentile) compared to tropical land. Tropical land has a slightly higher frequency outside this core distribution area, indicating more spread-out and diversified rain systems over the land regions. The higher frequency in the core distribution area in tropical oceans, on the other hand, indicates more abundant shallow convection that is limited in size and rain production. Compared to the PDFs in the tropics, the PDFs in subtropics show increased and decreased frequency on the left and right sides of the core distribution area, respectively (Figures 5c and 5d). This indicates that PFs in the subtropics have a slightly higher chance to be larger in size in the same rain percentiles, possibly due to relatively lower moisture content in the subtropics than in the tropics. There could be many reasons for large systems to occur in the relatively dry subtropics, i.e., the wave intrusion of cold fronts from higher latitudes and the organization of large MCSs under subtropical monsoonal flow (e.g., the Mei-yu front in China, MCSs over India and Argentina). The warm ocean currents in the subtropics may also contribute to the organization of large systems over oceans. Some mesoscale systems, such as hurricanes, are organized more easily off the equator due to the presence of the Coriolis force.

[22] The relationship between PF size and VRR is further illustrated in terms of mean conditional rain rates, defined as the ratio of VRR to PF size (Figure 6a). Surprisingly, mean conditional rain rates from all four subregions are rather close to each other and increase gradually from less than 5 mm/h in

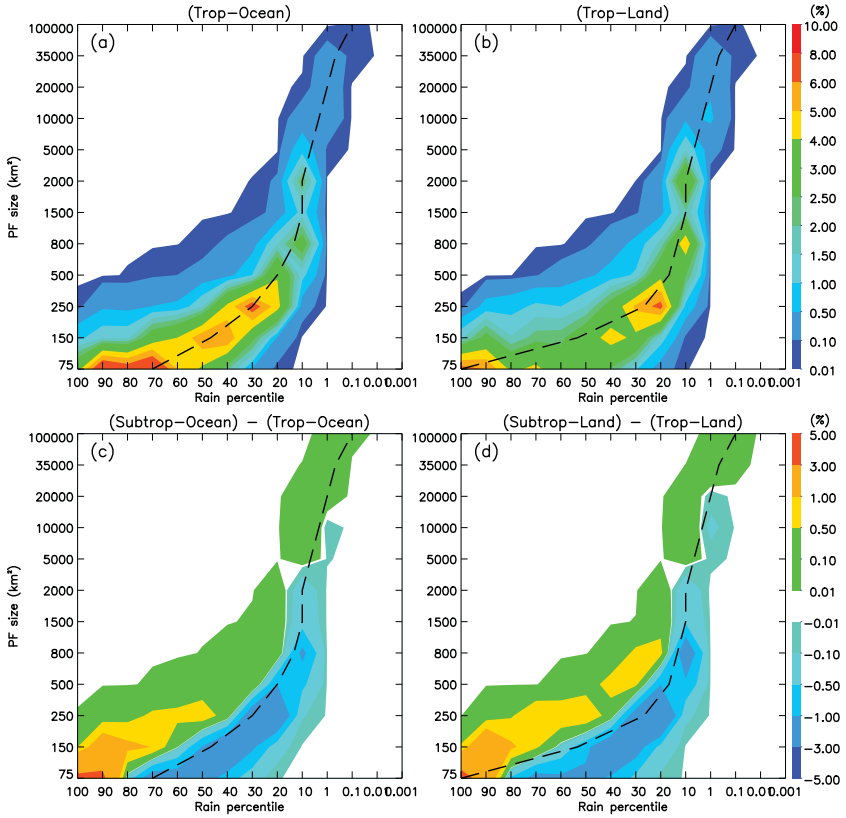


**Figure 5.** Two-dimensional histogram of PFs with size and total volumetric rain for (a) tropical ocean and (b) tropical land; (c) difference between subtropical ocean and tropical ocean; (d) same as Figure 5c but for land. Dashed lines indicate locations of maximum frequency.

small PFs (< top 10th percentile) to around 7 mm/h in extreme PFs. However, mean rain rates in convective and stratiform areas have quite different characteristics. The mean rain rates in convective areas increase from around 1 mm/h in PFs with low VRR to around 4–6 mm/h in the top 20th percentile and then increase rapidly to nearly 20 mm/h in the largest PFs (Figure 6a, blue lines). Compared to other regions, tropical oceans have relatively lower mean convective rain rates for PFs up to 1% but relatively higher mean convective rain rate for PFs larger than 1%. The mean rain rates in the stratiform areas are much smaller than those of the convective areas, starting from around 0.6 mm/h in the smallest PFs to around 5 mm/h in the largest PFs (Figure 6a, red lines). Previous studies have found that the fraction of convective rain area is a major factor in determining the mean conditional rain rate [*Nesbitt and Zipser*, 2003]. Figure 6b shows larger differences in convective rain area for smaller PFs ranging from 20% in subtropical land to 60% in tropical oceans. The differences become smaller as VRR increases, and convective areas in all regions except subtropical land drop to less than 15% as small systems develop into large organized systems with extended stratiform rain area. As a result, mean conditional rain rates are dominated by stratiform rain area for the large PFs, while they are not far apart from both convective and stratiform rain rates for small PFs. Even though there is a rapid increase of convective rain rate and a rapid decrease of convective rain area at 10%–1%, a much smoother change of the mean conditional rain rate across different PF sizes is found (Figure 6a, black lines).

[23] Besides the reverse trend in convective rain rate and area with VRR for all regions, there are regional compensating effects which further reduce the differences in conditional rain rate. For example, tropical oceans have the smallest convective rain rates and largest convective rain areas for smaller PFs but the largest convective rain rates and next to smallest convective rain areas for larger PFs. Subtropical land is the opposite of tropical oceans, having the smallest convective rain areas and the largest convective rain rates for smaller PFs but the largest convective rain areas and the smallest convective rain rates for larger PFs. Our results show that even with the decrease of fractional convective rain area, the conditional rain rates for both convective areas and stratiform areas increase with the PF size, which contribute to an overall increase in the mean total conditional rain rates across different PF sizes (Figure 6a). This is contradictory to *Nesbitt and Zipser* [2003], who showed that mean conditional rain rates in convective areas and stratiform areas are nearly constant throughout the day, while the change in convective fraction contributes to the diurnal cycle of mean conditional rain rate in different rain systems.

### 3.6. Variation of Rain Structure With VRR

[24] In this subsection, we further investigate the evolution of rain characteristics as a function of rain volume. To illustrate the significant departure of extreme PFs from the lower 99% of the rain systems, we show the changes of mean parameters that describe the vertical extension and rain intensity of the PF with VRR (Figure 7). Figure 7a shows that the

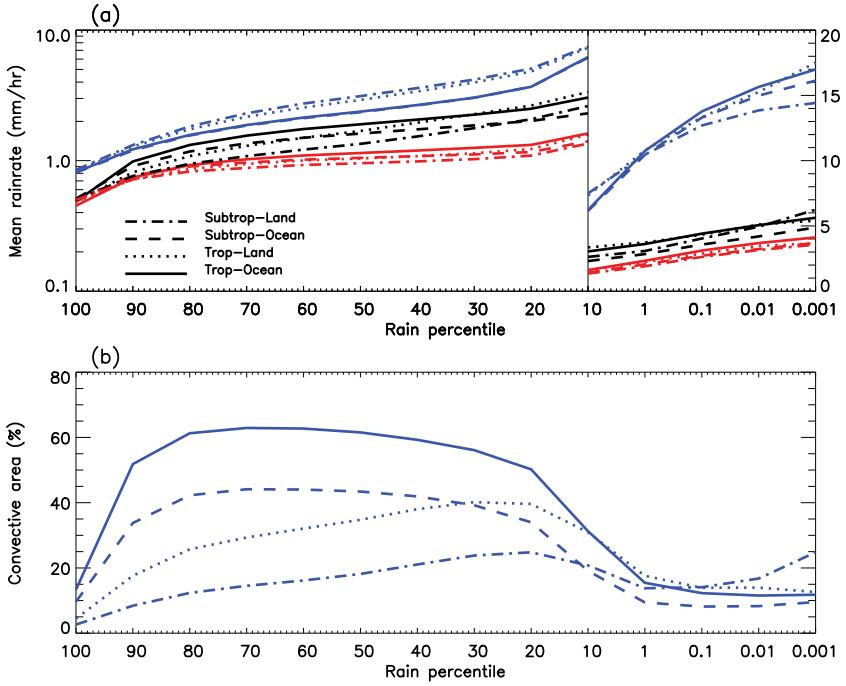


**Figure 6.** (a) Mean conditional rain rate for all (black), convective (blue), and stratiform (red) rain areas. The *y* axis is in logarithmic scale for PFs smaller than 10% and in linear scale for PFs larger than 10%. (b) Percentages of convective rain area. Line type indicates four different subregions.

mean minimum IR temperature (MinIR) separates into two groups (land and ocean) for the small PFs at around 250 and 265 K, respectively, with no latitudinal delineation. This indicates that smaller PFs over the ocean reach lower altitude compared to those over land (see also Figures 8a and 8b). The MinIR drops to below 220 K at the 10th percentile, and the difference between the tropics and subtropics starts to emerge in place of land and ocean, with MinIR in the tropics being 10 ~ 20 K colder than MinIR in the subtropics due to much higher and colder tropopause in the former. The mean maximum height (Maxht, Figure 7b) and mean maximum 40 dB*Z* (Maxht40, Figure 7c) also show a dramatic increase of storm height as VRR reaches the 10%–1% range. The mean storm height for small PFs also delineates by land and ocean at 3.5 and 5.5 km, respectively, but tend to merge as all of them rise to above 15 km for the most extreme PFs. Most small PFs are too weak to produce a 40 dB*Z* radar signal, so the mean Maxht40 is near zero until the 40th percentile but rises rather dramatically at 10%–1% to above 4 km for the most extreme PFs.

[25] The 85 GHz PCT reflects scattering signals of ice hydrometeors (graupel and hail) from convective updrafts above the freezing level [*Spencer et al*., 1989]. The minimum 37 GHz PCT is sensitive to larger hydrometers and can be used to identify low-level rain systems that are obscured by the precipitation-sized ice particles aloft. Both minimum 85 and 37 GHz PCTs show significant depression for the extreme PFs starting at the 10th percentile, indicating deep convection and strong ice scattering signals from the larger systems (Figures 7b and 7d). Lightning flash rates are highly correlated with convective ice water paths [*Petersen and Rutledge*, 1998; *Petersen et al*., 2005]. The mean flash rate also begins to increase at the 10th percentile, with much higher flash rates over the land than over the oceans for the PFs with similar VRR (Figure 7c). In all the cases, PFs over land have stronger convective intensity proxies than those over the oceans for the same VRR, consistent with much stronger convection over land. All parameters examined show dramatic change when VRR reaches a threshold of the 10th percentile (2300 mm/h km$^2$).

[26] Even though the mean characteristics of PFs show a systematic change with VRR, a large standard deviation is expected for any parameter at any given rain range. Figure 8 shows a two-dimensional histogram of Maxht versus MinIR for small (below the 20th percentile), intermediate (20%–1%) and large (above 1%) PFs over land and ocean, respectively. Over the oceans, the majority of PFs below the 20th percentile show a typical characteristic of shallow warm convection with storm heights at 2–4 km and cloud tops below or near the freezing level. Some of the small PFs could be as high as 8 km and colder than 200 K and identifiable as isolated cells disconnected from large systems. The small PFs over the land are both higher and colder than their oceanic counterpart, with the highest frequency appearing at 5 km and 260 K. The 20%–1% range corresponds to a transition spectrum, with PFs ranging from warm and shallow systems to deep and cold systems. PFs in the top 1% span from middle congestus to deep convection, with consistent maximum height and minimum IR and land regions showing higher concentrations of deeper convection. Note that shallow systems with large VRR do occur over several specific regions of frequent deep convection such as the East Pacific ITCZ [*Liu and Zipser*, 2009, 2013a].

### 3.7. Seasonal Variations of Extreme PF Characteristics

[27] The large spread in the 2-D histogram (Figure 8) is partly due to a multitude range of precipitation systems and

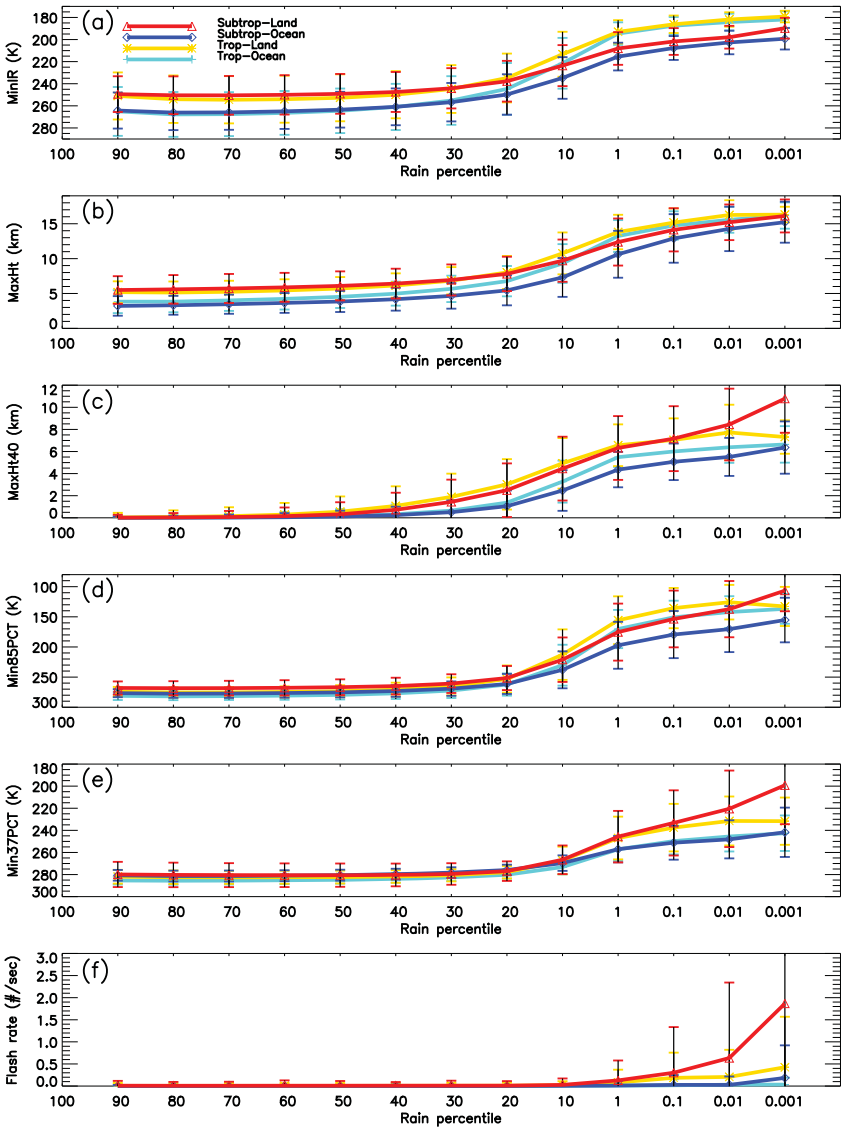


**Figure 7.** Mean values with one standard deviation error bars of (a) minimum infrared brightness temperature (MinIR), (b) maximum echo top height (Maxht), (c) maximum height of 40 dB*Z* (Maxht40), (d) minimum 85 GHz polarization correction temperature (Min85PCT), (e) minimum 37 GHz polarization corrected temperature (Min37PCT), and (f) flash rate for different percentiles of PFs. Note that for PFs without 40 dB*Z* echo, we used zero value in the average in Figure 7c.

partly due to variations in the large-scale environment that dominates precipitation systems in different geographical locations and different seasons. In this subsection, we will examine more detailed rain characteristics of extreme PFs in different subregions and different seasons. For plotting reasons, only data from the Northern Hemisphere are used in the figures in this subsection (Figures 9–11).

[28] Figure 9 shows the same 2-D histogram of Maxht versus MinIR as Figure 8 but isolates the top 1% of extreme PFs in boreal winter (DJF) and summer (JJA) separately in four subregions. There are obvious differences in rain characteristics between tropics and subtropics and between winter and summer in the subtropics. The rain characteristics for the top 1% of extreme PFs in the tropics are remarkably similar in echo top height and cloud top temperature between the land and oceans (also shown in Figures 7a and 7b) and between summer and winter seasons, with almost complete overlap of the DJF and JJA contours. Extreme PFs in the subtropics during summer resemble those in the tropics with a maximum frequency of distribution located at 14 km and 190 K, but extreme PFs in winter subtropics are significantly lower (6–8 km), with much warmer cloud top temperatures (210–220 K), which indicates very different rain systems such as cold fronts.

[29] Figure 10 further shows the vertical distributions of raining area (represented by area with 20 dB*Z* radar signal) for the top 1% of extreme PFs. It is interesting to note that the largest 20 dB*Z* area does not occur at the surface but at about 2 km above the ground. The surface raining area is substantially smaller, with only about 30 ~ 60% of the area at 2 km height. There are two possible reasons for this. One is that the raining area identified by TRMM PR is

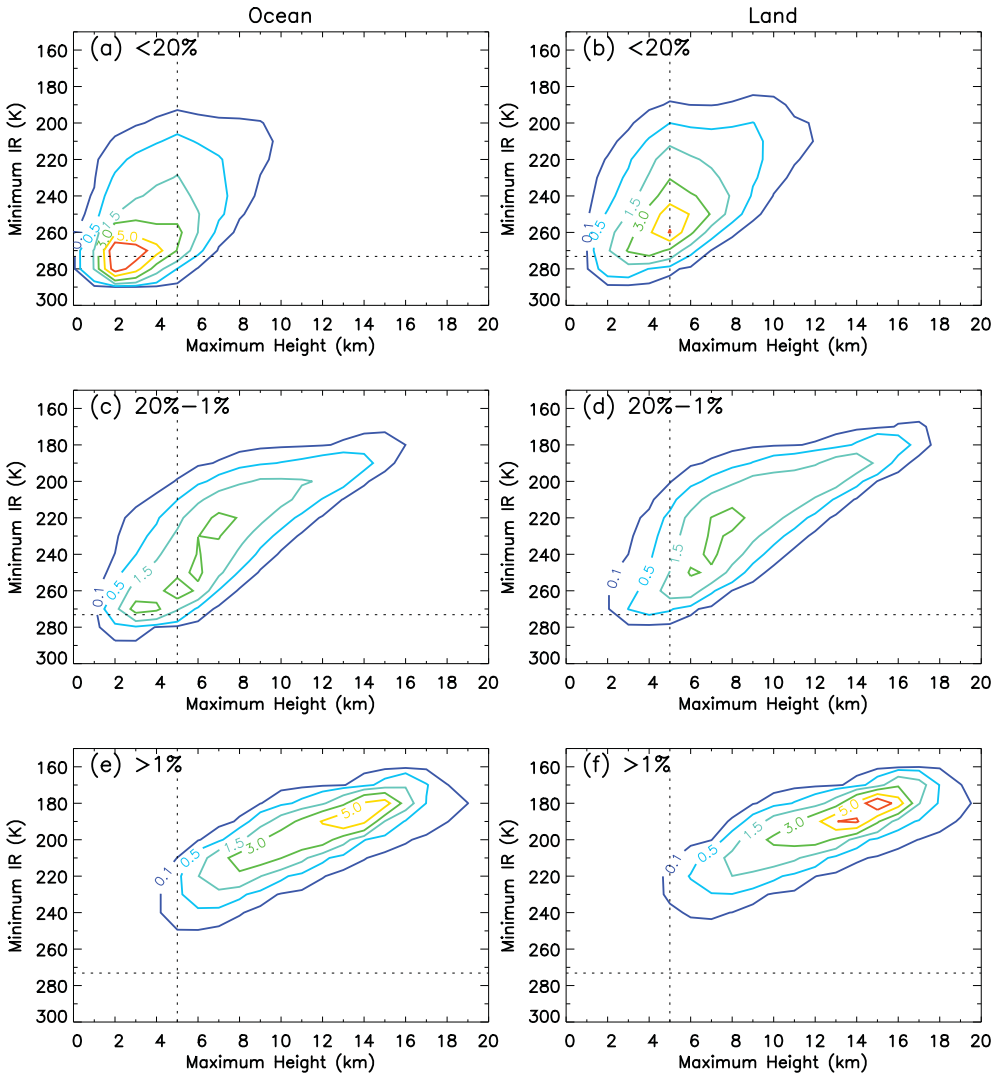


**Figure 8.** Two-dimensional histogram of minimum IR versus maximum storm height for PFs in (a, b) <20%, (c, d) 20–1%, and (e, f) >1% categories over oceans and land, respectively.

obtained from near-surface reflectivity measurements, which are valid PR observations at the lowest altitudes. Often, the PR profiles do not reach below 2 km because of ground clutter contamination. Just the lack of observations would lead the 20 dB$Z$ area near the surface to be smaller, but a second possible reason is that evaporation of rainfall in the stratiform regions could also reduce the reflectivity near the surface. From 2 km and above, the 20 dB$Z$ area decreases quickly to less than $2 \times 10^4$ km toward 8 km. The tropical rain systems extend higher vertically than the subtropical systems but narrower horizontally at the surface and near the surface. Tropical oceans have slightly lower vertical extension but larger rain area at lower altitudes than the tropical land even though maximum raining areas (0.1% contour) in both regions are very close in DJF. Tropical oceans also show an increased number of events with near-surface rain areas larger than $3 \times 10^5$ km$^2$ in JJA, which does not occur in the tropical land. Both subtropical land and oceans have small PF rainy areas at high altitudes (above 8 km) but have large areas at lower altitudes (below 5 km), with PFs in winter substantially larger than in summer (indicating broader and shallower frontal systems in winter).

[30] The Contour Frequency Altitude Diagram (CFAD) of maximum dB$Z$ shows that extreme tropical land events have stronger intensity, with higher maximum reflectivity values than those over the oceans (Figures 11a and 11b). At levels below freezing (~4.5 km in tropics), the slopes of the reflectivity increase toward the surface over the oceans but remain nearly vertical over land. This is possibly related to the difference in convective intensity between land and oceans [*Liu and Zipser*, 2013b]. Tropical land has fewer contour levels in the center of the distribution than the tropical oceans (Figures 11a and 11b), which is consistent with more spread and diversified rain system over tropical land (Figure 5). There is negligible difference in the vertical rain intensity between winter and summer in the tropics, but significant difference can be found in subtropical winter and summer (Figures 11c and 11d). Here the vertical distributions of the maximum radar signals of subtropical land and oceans in JJA again resemble those of the tropics, but the DJF contours show a unique double peak feature: one with a maximum

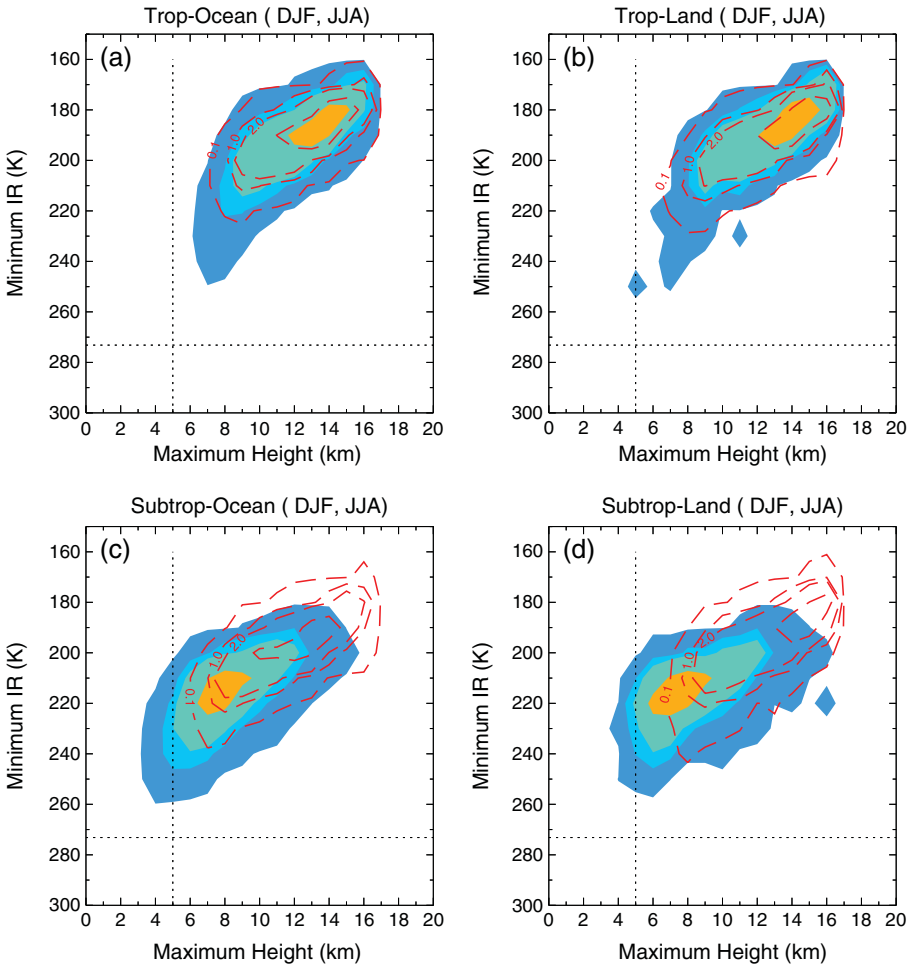


**Figure 9.** Two-dimensional histogram of minimum IR versus maximum storm height for the top 1% of extreme events in DJF (shading) and JJA (contour) in four subregions.

radar signal of 45–50 dB*Z* extending from near the surface to about 4–5 km in altitude (consistent with strong surface rain intensity from these extreme PFs) and the other with a maximum radar signal of 25–30 dB*Z* located at 5–6 km above the ground. The latter peak should not be identified as a bright band because it is located above the freezing level (which is typically lower than 4.5 km in winter over the subtropics) and the maximum radar reflectivity of a PF usually comes from the convective region of the system where the bright band is not clearly detected. In fact, this strongly suggests dominant shallow frontal systems with a convective cloud top reaching only 7–9 km.

[31] The separation of tropical and extratropical rain systems based on geographical boundaries (20° north and south) will inevitably misidentify some rain systems. For example, some of the PFs in the tropical region may have moved from the extratropics and vice versa. We followed *Xu et al.* [2007], using an eddy growth parameter σ as a baroclinic instability criterion to physically separate the tropical and extratropical rain systems. The eddy growth parameter is computed as $\sigma = 0.31 \times f/N \times (d|V|/dZ)$, where f is the Coriolis parameter, N the Brunt–Väisälä frequency, and d|V|/dZ is computed from winds at 1000 and 700 hPa. If σ is greater than 0.1/day, the system is considered to be baroclinic and extratropical in nature; otherwise, it is considered tropical. As a result, we found that about 10% and 18% of PFs in DJF in subtropical land and oceans, respectively, may belong to tropical systems because of their small baroclinic instability. In JJA, nearly half of the PFs do not meet the baroclinic instability criterion. However, the structural difference with respect to the baroclinic criterion is rather insignificant in the subtropical regions. In the tropical regions (0°N–20°N), about 20–30% of PFs meet the baroclinic criterion and may be considered to be extratropical systems. We notice that the PFs with larger baroclinic instability in the tropics are relatively larger in size and have lower maximum dB*Z* levels (figures not shown), which are consistent with the overall results from Figures 10 and 11.

[32] The above results (Figures 9–11) show that extreme PFs in the tropics extend higher with stronger rain intensity than the subtropical rain systems and experience very little seasonal variation. Summertime extreme PFs in the subtropics, characterized by smaller rain areas but thicker and heavier vertical rain volumes, resemble those in the tropics and is consistent with more locally convective-driven systems. Wintertime subtropical extreme PFs are lower and broader, indicating characteristics of frontal rain systems. Of all the subregions studied, seasonal variation is most significant in subtropical land.

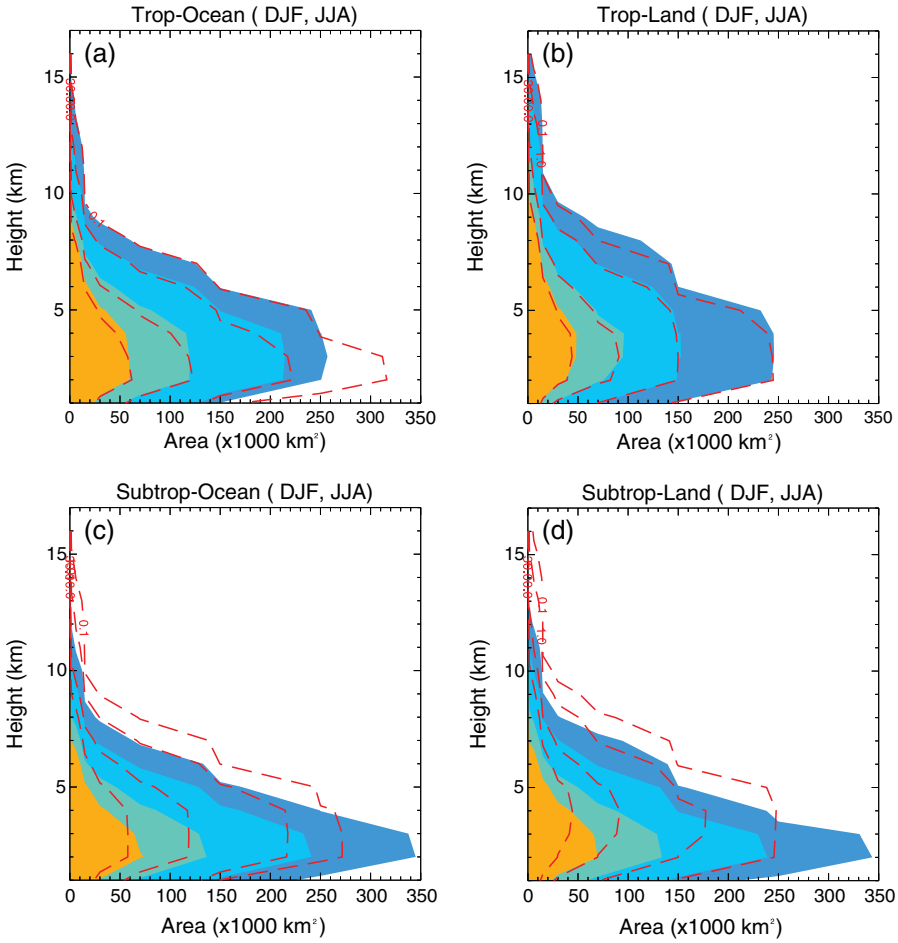


**Figure 10.** Cumulative frequency with altitude (CFADs) of the area with 20 dB*Z* for the top 1% of extreme events in DJF (shading) and JJA (contour) in four subregions.

## 4. Large-Scale Environment

[33] Many studies have attempted to characterize typical meteorological conditions and major patterns of precipitation systems associated with extreme precipitations on a regional basis [*Maddox et al*., 1979; *Glass et al*., 1995; *Doswell et al*., 1996; *Moore et al*., 2003; *Schumacher and Johnson*, 2005; *Romatschke and Houze*, 2010, 2011a, 2011b]. The synoptic and mesoscale environments of extreme precipitation from different geographical regions and for different storm types can be quite varied. Here we composite the large-scale environments for different percentiles of PFs to see if such systematic changes exist. We show 500 hPa relative humidity, total precipitable water, 500 hPa vertical velocity, vertical wind shear, and convective available potential energy (CAPE) in particular to represent atmospheric thermodynamic, dynamic, and convective potentials, respectively.

[34] Figure 12a shows that mean precipitable water remains constant for PFs below the top 10th percentile but increases rapidly after the PFs reach the 10th percentile and beyond, suggesting that increased total precipitable water is essential to extreme rainfall. There is a clear separation of the total precipitable water between the tropics and subtropics regardless of land or ocean, with the tropics being about 15 mm higher than the subtropics due to warmer temperature and higher specific humidity. The differences narrow as the mean precipitable water in all regions reaches around 50 mm for the extreme PFs. It is interesting to notice that the 500 hPa mean relative humidity over land is slightly higher than the relative humidity over the oceans for small PFs between the 90th and 10th percentiles, indicating that for small precipitations to occur, the moistening of the free atmosphere is even more important over land than over the oceans. The mean 500 hPa relative humidity rises rapidly with rainfall in all the regions until the PF reaches the critical threshold of the 10th percentile but levels off for the most extreme ones in the subtropics (Figure 12b). The surge of midlevel relative humidity for extreme PFs is likely related to the large-scale moisture convergence and convective uprising that brings in additional moisture to that level.

[35] The rapid increase in relative humidity for the extreme PFs is well correlated with an increase in 500 hPa vertical velocities. Similar to relative humidity, the mean 500 hPa vertical velocity remains constant at around 0.1 Pa/s for small PFs up to the 10th percentile, then increases abruptly after the 10th percentile and reaches tenfold in magnitude in the top 0.01% compared to those in the lower 90% (Figure 12c). For extreme PFs, subtropical storms have higher vertical velocity compared to tropical storms, which might be due to stronger convergence and vertical motions, both required to support the required moisture convergence in the relatively dry area (less total precipitable water in subtropics). It is well

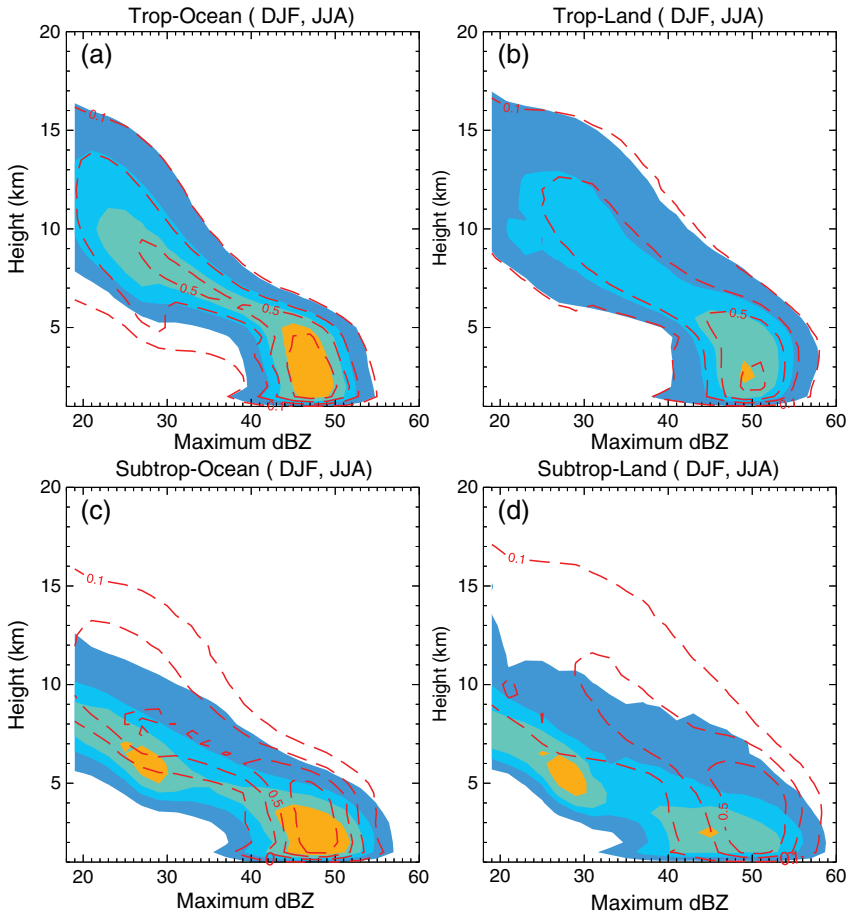


**Figure 11.** Contoured frequency by altitude diagrams (CFADs) of maximum PR reflectivity for the top 1% of extreme events in DJF (shading) and JJA (contour) in four subregions.

known that precipitation at any given location comes from evaporation and moisture convergence. For heavy precipitation, moisture convergence is far more important than local evaporation. The rapid increase of midlevel relative humidity and vertical velocity shows that large-scale dynamics plays a critical role to local precipitation [*O'Gorman and Schneider*, 2009; *Chou et al*., 2012].

[36] Besides atmospheric moisture and vertical velocity, which are directly related to extreme precipitation, many other environmental factors could affect the generation, intensity, and duration of precipitation systems. For example, large environmental vertical wind shear hinders tropical cyclone development but favors multicell systems in the subtropics. Strong ambient vertical shear is found to be very important to the structure, strength, and longevity of subtropical squall lines over land [*Bluestein and Jain*, 1985; *Rotunno et al*., 1988; *Weisman and Rotunno*, 2004]. To examine whether vertical wind shear affects rain volume in any systematic manner, we plotted mean vertical shears between 250 and 850 hPa for different percentiles of PFs (Figure 12d). It is not surprising to see that mean vertical wind shear values over the subtropics are much higher than those over the tropics due to a more baroclinic atmosphere in general. Vertical shear varies little for the small PFs for all the regions. However, they start to increase at the 10th percentile in subtropical land and oceans, indicating larger vertical shear is conducive to some subtropical storm systems. Vertical wind shear in both tropical land and oceans remains constant for the entire rain spectrum even with the known effects on tropical cyclones, probably due to the small percentage of tropical cyclone-related PFs of the total PFs.

[37] The last environmental parameter examined is related to the atmospheric instability, i.e., convective available potential energy (CAPE). Since convective related precipitation is due to buildup of atmosphere instability, precipitation through vertical overturning and latent heat release will remove or reduce that instability. Figure 12e shows large differences in the mean CAPE from different regions; the mean CAPEs over subtropical land and oceans are much smaller than those of the tropics due to a large number of subtropical systems having very small or no CAPE. The CAPE generally increases slightly with PF percentiles up to 10% for all the regions but only continues increasing slowly for extreme PFs in tropical oceans. For the subtropical land region, there is a discernible decreasing trend of CAPE from around 850 J/kg at the top 10% to around 650 J/kg at the top 0.01%, which is likely due to the release of some of the prestorm instability in these large mature systems. However, it should be noted that CAPE is a loose measure of atmospheric instability and the standard deviation is very large (~700 J/kg). How effective the instability can be converted into actual convective activity (i.e., vertical velocity and rainfall) depends on many factors such as large-scale moisture convergence, convective inhibition, midlevel moisture, wind shear, and entrainment

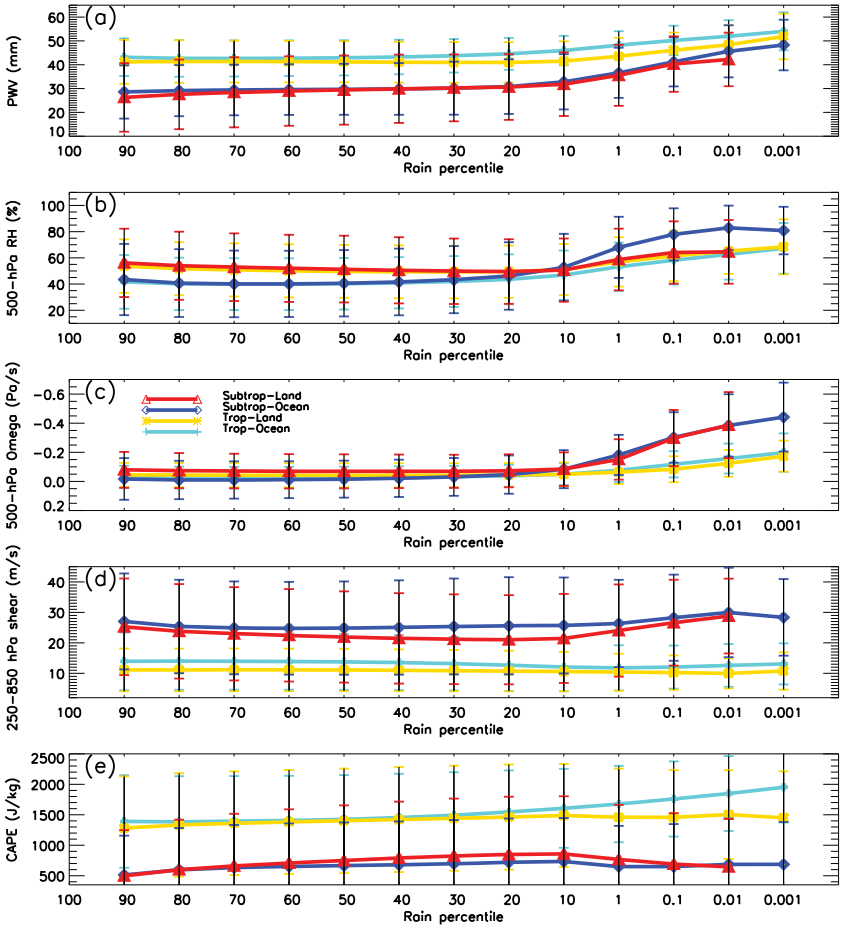


**Figure 12.** Mean values with one standard deviation error bars of (a) 500 hPa relative humidity, (b) total precipitable water vapor, (c) 500 hPa vertical velocity, (d) 200–850 hPa wind shear, and (e) CAPE from NCEP reanalysis for PFs with different percentile of volumetric rainfall.

[*Lucas et al.*, 1994]. Therefore, we should expect a generally weak relationship between VRR and CAPE and that the same CAPE would work differently over different regions. In addition, due to the temporal interpolation and coarse horizontal resolution, there is a large uncertainty in the CAPE computed from the NCEP reanalysis, especially for small PFs. As a result, these relationships should be considered qualitative in nature.

[38] This section shows very nonlinear behavior of the large-scale parameters that experience little change for the lower 90% of PFs but change rapidly after the 10th percentile. These environmental conditions are directly related to the observed abrupt changes in the structure of the PF, which is likely caused by convective-driven vertical motion accompanied by large-scale moisture convergence and the release of CAPE.

## 5. Summary and Discussions

[39] This study adopts a "precipitation object" approach by using the Precipitation Feature (PF) database developed at the University of Utah to analyze the characteristics and large-scale environment of extreme precipitation from 14 year TRMM observations. We define extreme PF with the volumetric rain of the PF in order to capture the effect of both spatial extent and rain intensity. We have found that instantaneous PFs have much larger dynamic ranges than the daily gridded precipitation, with those in the top 1% being 2 orders of magnitude larger than the medium PFs and contributing to over 55% of instantaneous rainfall. Ninety percent of the PFs that contribute about 20% of total precipitation belong to meso-γ systems (less than 20 km in the horizontal direction) or broken patches from large systems. The most abrupt change is found to be around the top 10%–1%, where the rain systems expand from a few hundred to a few thousand kilometers in size and from 2300 to 40,000 mm/h km$^2$ in rain volume. Spatial and temporal distributions and the mean characteristics of extreme PFs are discussed in comparison to intermediate and smaller PFs. We find that regional differences in rain characteristics mainly come from land-ocean differences for smaller PFs. As the VRR of PF increases, the regional differences mainly come from the tropics and subtropics. While extreme PFs in the top 1% are found to be significantly larger, deeper, and colder than the lower 90% of PFs, extreme PFs in the tropics are even deeper and colder than the subtropical systems and present no significant seasonal variations. The extreme PFs in the subtropics in the summertime resemble those in the tropics, characterized by locally convection-driven rain systems. The extreme PFs in subtropical winter are much broader and shallower, which

is a signature of midlatitude frontal systems. The NCEP reanalysis shows that midlevel relative humidity and total precipitable water increase consistently with increasingly larger rain systems, along with sharp increases of upward vertical velocities to provide necessary dynamic support. Instantaneous CAPE also generally increases with larger PF, but the mean CAPE levels off for the extremely large systems due to the release of CAPE in mature systems in subtropical land regions. The study illustrates important roles of large-scale moisture and dynamic conditions for occurrences of extreme precipitation.

[40] It has been widely accepted that increasing moisture in the atmosphere potentially provides a mechanism for increasing extreme precipitation in a warming climate [*Trenberth et al*., 2003; *Allan and Soden*, 2008]. However, the correlation between surface temperature, atmospheric water vapor, and precipitation is not always positive and is highly dependent on the regions and time scales [*Adler et al*., 2008; *Gu and Adler*, 2011]. In addition, both observations and climate model simulations show that increases in extreme precipitation do not always follow the rate of increase in atmosphere water content [*Lau and Wu*, 2011]. Therefore, it is important to confirm that the total water vapor in the atmosphere is indeed highly correlated to the total volumetric rainfall, even on an instantaneous basis. This proves that extreme rainfall is more likely to occur when high water vapor content is readily available in the atmosphere.

[41] This study, as well as previous studies [*Doswell et al*., 1996; *Schumacher and Johnson*, 2005], points out the necessary conditions for extreme precipitation to occur, such as high atmospheric water vapor, high upward vertical velocity, and high atmospheric moist static energy. It is tempting to consider that each of these meteorological parameters can reach their optimum statuses when a precipitation system is organized, which might have no direct connection to global warming. However, it has been shown that it is the thermodynamic effect rather than the dynamic effect that is considered mainly responsible for changes in precipitation intensity [*Allan and Soden*, 2008; *Emori and Brown*, 2005; *O'Gorman and Schneider*, 2009; *Chou et al*., 2012]. Thus, water vapor in the atmosphere is the most relevant parameter related to the effect of global warming. This study shows a consistent increase of mean volumetric rainfall with the increase of total precipitable water in the real world, which could imply that there is more extreme rain in a warming climate when atmospheric water vapor loading is high.

[42] Obviously, there are large standard deviations for the mean characteristics and large-scale environments for all percentiles of the PFs. This is not a surprise because many different types of rain systems occur in each location and nature never repeats itself. Therefore, these results should be interpreted as qualitative rather than quantitative. The other caveat is related to the instantaneous nature of PFs; some of the extreme PFs do not produce extreme rainfall accumulation. However, our results are based on a large number of PF samples over the global tropics; thus, the observed systematic changes of the rainfall characteristics and large-scale parameters associated with extreme PFs are fundamental to understanding the mechanisms of development of extremes in current and future climates.

[43] **Acknowledgments.** This work is supported by the Precipitation Measuring Mission under project NNX13AF73G (Headquarter Manager: R. Kakar), NASA Earth Science Division. The authors thank the reviewers' many constructive comments that helped improve the manuscript.

## References

Adler, R. F., G. Gu, G. J. Huffman, J. J. Wang, S. Curtis, and D. T. Bolvin (2008), Relationships between global precipitation and surface temperature on interannual and longer timescales (1979–2006), *J. Geophys. Res.*, *113*, D22104, doi:10.1029/2008JD010536.

Allan, R. P., and B. J. Soden (2008), Atmospheric warming and the amplification of precipitation extremes, *Science*, *321*, 1481–1484, doi:10.1126/science.1160787.

Allen, M. R., and W. J. Ingram (2002), Constraints on future changes in climate and the 534 hydrologic cycle, *Nature*, *419*, 224–232.

Bluestein, H. B., and M. H. Jain (1985), Formation of mesoscale lines of precipitation: Severe squall lines in Oklahoma during the spring, *J. Atmos. Sci.*, *42*, 1711–1732.

Bowman, K. P., J. C. Collier, G. R. North, Q. Wu, and E. Ha (2005), Diurnal cycle of tropical precipitation in Tropical Rainfall Measuring Mission (TRMM) satellite and ocean buoy rain gauge data, *J. Geophys. Res.*, *110*, D21104, doi:10.1029/2005JD005763.

Bradley, A. A., and J. A. Smith (1994), The hydrometerological environment of extreme rainstorms in the southern plains of the United States, *J. Appl. Meteorol.*, *33*, 1418–1431.

Chou, C., C.-A. Chen, P.-H. Tan, and K.-T. Chen (2012), Mechanisms for global warming impacts on precipitation frequency and intensity, *J. Clim.*, *25*, 3291–3306.

Dole, R., M. Hoerling, J. Perlwitz, J. Eischeid, P. Pegion, T. Zhang, X.-W. Quan, T. Xu, and D. Murray (2011), Was there a basis for anticipating the 2010 Russian heat wave?, *Geophys. Res. Lett.*, *38*, L06702, doi:10.1029/2010GL046582.

Doswell, C. A., III, H. E. Brooks, and R. A. Maddox (1996), Flash flood forecasting: An ingredients based methodology, *Wea. Forecasting*, *11*, 560–581.

Easterling, D. R., J. L. Evans, P. Ya Groisman, T. R. Karl, K. E. Kunkel, and P. Ambenje (2000), Observed variability and trends in extreme climate events: A brief review, *Bull. Am. Meteorol. Soc.*, *81*, 417–425.

Eitzen, Z. A., and K.-M. Xu (2005), A statistical comparison of deep convective cloud objects observed by an Earth Observing System satellite and simulated by a cloud resolving model, *J. Geophys. Res.*, *110*, D15S14, doi:10.1029/2004JD005086.

Emori, S., and S. J. Brown (2005), Dynamic and thermodynamic changes in mean and extreme precipitation under changed climate, *Geophys. Res. Lett.*, *32*, L17706, doi:10.1029/2005GL023272.

Ge, X., T. Li, S. Zhang, and M. S. Peng (2010), What causes the extremely heavy rainfall in Taiwan during Typhoon Morakot (2009)?, *Atmosph. Sci. Lett.*, *11*, 46–50.

Glass, F. H., D. L. Ferry, J. T. Moore, and S. M. Nolan (1995), Characteristics of heavy convective rainfall events across the Mid-Mississippi Valley during the warm season: Meteorological conditions and a conceptual model. Preprints, 14th Conf. on Weather Analysis and Forecasting, Dallas, TX, *Amer. Meteor. Soc.*, 34–41.

Groisman, P. Y., R. W. Knight, D. R. Easterling, T. R. Karl, G. C. Hegerl, and V. N. Razuvaev (2005), Trends in intense precipitation in the climate record, *J. Clim.*, *18*, 1326–1350, doi:10.1175/JCLI3339.1.

Gu, G., and R. F. Adler (2011), Large-scale, inter-annual relations among surface temperature, water vapour, *Inter. J. climatology*, doi:10.1002/joc.2393.

Heideman, K. F., and J. M. Fritsch (1988), Forcing mechanisms and other characteristics of significant summertime precipitation, *Wea. Forecasting*, *3*, 115–130.

Held, I. M., and B. J. Soden (2006), Robust responses of the hydrological cycle to global warming, *J. Clim.*, *19*, 5686–5699.

Houze, R. A., Jr., and D. D. Churchill (1987), Mesoscale organization and cloud microphysics in a Bay of Bengal depression, *J. Atmos. Sci.*, *44*, 1845–1868.

Houze, R. A., K. L. Rasmussen, S. Medina, S. R. Brodzik, and U. Romatschke (2011), Anomalous atmospheric events leading to the summer 2010 floods in Pakistan, *Bull. Am. Meteorol. Soc.*, doi:10.1175/2010BAMS3173.1.

Huffman, G. J., D. T. Bolvin, E. J. Nelkin, and D. B. Wolff (2007), The TRMM Multisatellite Precipitation Analysis (TMPA): Quasi-global, multiyear, combined-sensor precipitation estimates at fine scales, *J. Hydrometeor.*, *8*, 38–55.

Iguchi, T., T. Kozu, R. Meneghini, J. Awaka, and K. Okamoto (2000), Rain-profiling algorithm for the TRMM precipitation radar, *J. Appl. Meteorol.*, *39*, 2038–2052.

Iguchi, T., T. Kozu, J. Kwiatkowski, R. Meneghini, J. Awaka, and K. Okamoto (2009), Uncertainties in the rain profiling algorithm for the TRMM precipitation radar, *J. Meteor. Soc. Japan*, *87a*, 1–30.

IPCC (2012), Managing the risks of extreme events and disasters to advance climate change adaptation, *A Special Report of Working Groups I and II of the Intergovernmental Panel on Climate Change*, edited by C. B. Field et al., p. 582, Cambridge University Press, Cambridge, UK, and New York, NY, USA.

Kalnay, E., et al. (1996), The NCEP/NCAR 40-year reanalysis project, *Bull. Am. Meteorol. Soc.*, *77*, 437–471.

Kharin, V. V., F. W. Zwiers, X. Zhang, and G. C. Hegerl (2007), Changes in temperature and precipitation extremes in the IPCC ensemble of global coupled model simulations, *J. Clim.*, *20*, 1419–1444, doi:10.1175/JCLI4066.1.

Kistler, R., W. Collins, S. Saha, G. White, and J. Woollen (2001), The NCEP-NCAR 50-year reanalysis: Monthly means CD–ROM and documentation, *Bull. Am. Meteorol. Soc.*, *82*, 247–267, doi:10.1175/1520-0477(2001)082<0247:TNNYRM>2.3.CO;2.

Kraus, E. B. (1963), The diurnal precipitation change over the sea, *J. Atmos. Sci.*, *20*, 551–556.

Lau, W. K. M., and K.-M. Kim (2012), The 2010 Pakistan flood and Russian heat wave: Teleconnection of hydrometeorological extremes, *J. Hydrometeor*, *13*, 392–403.

Lau, K.-M., and H.-T. Wu (2007), Detecting trends in tropical rainfall characteristics, 1979–2003, *Int. J. Climatology*, *27*, 979–988.

Lau, K.-M., and H. T. Wu (2011), Climatology and changes in tropical oceanic rainfall characteristics inferred from Tropical Rainfall Measuring Mission (TRMM) data (1998–2009), *J. Geophys. Res.*, *116*, D17111, doi:10.1029/2011JD015827.

Lau, K.-M., Y. P. Zhou, and H.-T. Wu (2008), Have tropical cyclones been feeding more extreme rainfall?, *J. Geophys. Res.*, *113*, D23113, doi:10.1029/2008JD009963.

Lau, W. K. M., H.-T. Wu, and K.-M. Kim (2013), A canonical response of precipitation characteristics to global warming from CMIP5 models, *Geophys. Res. Lett.*, *40*, 3163–3169, doi:10.1002/grl.50420.

Lee, C.-S., C.-C. Wu, T.-C. Chen Wang, and R. L. Elsberry (2011), Advances in understanding the "perfect monsoon-influenced typhoon": Summary from International Conference on Typhoon Morakot (2009), *Asia-Pac. J. Atmos. Sci.*, *47*(3), 213–222.

Lin, B., B. A. Wielicki, P. Minnis, L. Chambers, X. Kuan-Man, H. Yongxiang, and A. Fan (2006), The effect of environmental conditions on tropical deep convective systems observed from the TRMM satellite, *J. Clim.*, *19*, 5745–5761, doi:10.1175/JCLI3940.1.

Lin, B., K.-M. Xu, P. Minnis, B. A. Wielicki, Y.-X. Hu, L. Chambers, T.-F. Fan, and W. Sun (2007), Coincident occurrences of tropical individual cirrus clouds and deep convective systems derived from TRMM observations, *Geophys. Res. Lett.*, *34*, L14804, doi:10.1029/2007GL029768.

Liu, C., and E. J. Zipser (2008), Diurnal cycles of precipitation, clouds, and lightning in the triopics from 9 years of TRMM observations, *Geophys. Res. Lett.*, *35*, L04819, doi:10.1029/2007GL032437.

Liu, C. (2011), Rainfall contributions from precipitation systems with different sizes, convective intensities, and durations over the tropics and subtropics, *J. Hydrometeor*, *12*, 394–412, doi:10.1175/2010JHM1320.1.

Liu, C., and E. J. Zipser (2009), "War rain" in the tropics: Seasonal and regional distribution based on 9 years of TRMM data, *J. Clim.*, *22*, 767–779.

Liu, C., and E. Zipser (2013a), Regional variation of morphology of the organized convection in the tropics and subtropics, part I: Regional variation, *J. Geophys. Res. Atmospheres*, *118*, 453–466, doi:10.1029/2012JD018409.

Liu, C., and E. Zipser (2013b), Why does radar reflectivity tend to increase downward toward the ocean surface, but decrease downward toward the land surface?, *J. Geophys. Res. Atmospheres*, *118*, 135–148, doi:10.1029/2012JD018134.

Liu, C., E. J. Zipser, D. J. Cecil, S. W. Nesbitt, and S. Sherwood (2008), A cloud and precipitation feature database from 9 years of TRMM observations, *J. Appl. Meteorol. Climatol.*, *47*, 2712–2728.

Lucas, C., E. J. Zipser, and M. A. LeMone (1994), Convective available potential energy in the environment of oceanic and continental clouds: Correction and comments, *J. Atmos. Sci.*, *51*, 3829–3830, doi:10.1175/1520-0469(1994)051<3829:CAPEIT>2.0.CO;2.

Maddox, R. A., C. F. Chappell, and L. R. Hoxit (1979), Synoptic and mesoscale aspects of flash flood events, *Bull. Am. Meteorol. Soc.*, *60*, 115–123.

Min, S.-K., X. Zhang, F. W. Zwiers, and G. C. Hegerl (2011), Human contribution to more-intense precipitation extremes, *Nature*, *470*(7334), 378–381, doi:10.1038/nature09763.

Mohr, K. I., J. S. Famiglietti, and E. J. Zipser (1999), The contribution to tropical rainfall with respect to convective system type, size, and intensity estimated from the 85-GHz ice-scattering signature, *J. Appl. Meteorol.*, *38*, 596–606.

Moore, J. T., F. H. Glass, C. E. Graves, S. M. Rochette, and M. J. Singer (2003), The environment of the warm-season elevated thunderstorms associated with heavy rainfall over the central United States, *Wea. Forecasting*, *18*, 861–878.

Nesbitt, S. W., and E. J. Zipser (2003), The diurnal cycle of rainfall and convective intensity according to three years of TRMM measurements, *J. Clim.*, *16*, 1456–1475.

Nesbitt, S. W., E. J. Zipser, and D. J. Cecil (2000), A census of precipitation features in the tropics using TRMM: Radar, ice scattering, and lightning observations, *J. Clim.*, *13*, 4087–4106.

O'Gorman, P. A., and T. Schneider (2009), The physical basis for increases in precipitation extremes in simulations of 21st-century climate change, *Proc. Natl. Acad. Sci.*, *106*, 14,773–14,777.

Petersen, W. A., and S. A. Rutledge (1998), On the relationship between cloud-to-ground lightning and convective rainfall, *J. Geophys. Res.*, *103*, 14,025–14,040.

Petersen, W. A., L. D. Carey, S. A. Rutledge, J. C. Knievel, and R. H. Johnson (1999), Mesoscale and radar observations of the Fort Collins flash flood of 28 July 1997, *Bull. Am. Meteorol. Soc.*, *80*, 191–216.

Petersen, W. A., H. J. Christian, and S. A. Rutledge (2005), TRMM observations of the global relationship between ice water content and lightning, *Geophys. Res. Lett.*, *32*, L14819, doi:10.1029/2005GL023236.

Pontrelli, M. D., G. Bryan, and J. M. Fritsch (1999), The Madison County, Virginia, flash flood of 27 June 1995, *Wea. Forecasting*, *14*, 384–404.

Reale, O., K. M. Lau, J. Susskind, and R. Rosenberg (2012), AIRS impact on analysis and forecast of an extreme rainfall event (Indus River Valley, Pakistan, 2010) with a global data assimilation and forecast system, *J. Geophys. Res.*, *117*, D08103, doi:10.1029/2011JD017093.

Romatschke, U., and R. A. Houze Jr. (2010), Extreme summer convection in South America, *J. Clim.*, *23*, 3761–3791.

Romatschke, U., and R. A. Houze Jr. (2011a), Characteristics of precipitating convective systems in the premonsoon season of South Asia, *J. Hydrometeorol.*, *12*, 157–180.

Romatschke, U., and R. A. Houze Jr. (2011b), Characteristics of precipitating convective systems in the South Asian Monsoon, *J. Hydrometeorol.*, *12*, 3–26.

Rotunno, R., J. B. Klemp, and M. L. Weisman (1988), A theory for strong, long-lived squall lines, *J. Atmos. Sci.*, *45*, 463–485.

Schumacher, R. S., and R. H. Johnson (2005), Organization and environmental properties of extreme-rain-producing mesoscale convective systems, *Mon. Weather Rev.*, *133*, 961–976, doi:10.1175/MWR2899.1.

Shepherd, J. M., A. Grundstein, and T. L. Mote (2007), Quantifying the contribution of tropical cyclones to extreme rainfall along the coastal southeastern United States, *Geophys. Res. Lett.*, *34*, L23810, doi:10.1029/2007GL031694.

Smith, J. A., M. L. Baeck, Y. Zhang, and C. A. Doswell (2001), Extreme rainfall and flooding from supercell thunderstorms, *J. Hydrometeorol.*, *2*(5), 469–489.

Spencer, R. W., H. Michael Goodman, and R. E. Hood (1989), Precipitation retrieval over land and ocean with the SSM/I: Identification and characteristics of the scattering signal, *J. Atmos. Oceanic Technol.*, *6*, 254–273, doi:10.1175/1520-0426(1989)006<0254:PROLAO>2.0.CO;2.

Takayabu, Y., et al. (2012), How can we detect extreme rainfalls from the satellite data?, 18th Conference on Satellite Meteorology, Oceanography and Climatology/ First Joint AMS-Asia Satellite Meteorology Conference, New Orleans, January 25.

Trenberth, K. E., A. Dai, R. M. Rasmussen, and D. B. Parsons (2003), The changing character of precipitation, *Bull. Am. Meteorol. Soc.*, *84*, 1205–1217.

Wang, S. Y., R. E. Davis, W. R. Huang, and R. R. Gilllies (2011), Pakistan's two-stage monsoon and links with the recent climate change, *J. Geophys. Res.*, *116*, D16114, doi:10.1029/2011JD015760.

Weisman, M. L., R. Rotunno (2004), "A theory for strong long-lived squall lines" revisited, *J. Atmos. Sci.*, *61*, 361–382, doi:10.1175/1520-0469(2004)061<0361:ATFSLS>2.0.CO;2.

Xu, K.-M., T. Wong, B. A. Wielicki, L. Parker, and Z. A. Eitzen (2005), Statistical analyses of satellite cloud object data from CERES. Part I: Methodology and preliminary results of the 1998 El Niño/2000 La Niña, *J. Clim.*, *18*, 2497–2514.

Xu, K.-M., T. Wong, B. A. Wielicki, L. Parker, B. Lin, Z. A. Eitzen, and M. Branson (2007), Statistical analyses of satellite cloud object data from CERES. Part II: Tropical convective cloud objects during 1998 El Niño and evidence for supporting the fixed anvil temperature hypothesis, *J. Clim.*, *20*, 819–842.

Yang, G.-Y., and J. Slingo (2001), The Diurnal Cycle in the Tropics, *Mon. Wea. Rev.*, *129*, 784–801.

Zhang, X., L. Alexander, G. C. Hegerl, P. Jones, A. K. Tank, T. C. Peterson, B. Trewin, and F. W. Zwiers (2011), Indices for monitoring changes in extremes based on daily temperature and precipitation data, *WIREs Clim. Change*, *2*, 851–870, doi:10.1002/wcc.147.

Zipser, E., D. Cecil, C. Liu, S. W. Nesbitt, and D. Yorty (2006), Where are the most intense thunderstorms on Earth?, *Bull. Am. Meteorol. Soc.*, *87*, 1057–1071.